Experimental Investigation of the Grade Efficiency of a Zigzag Separator

Eduard Lukas[a], Christoph Roloff[b], Dominique Thévenin[b], Berend van Wachem[a,*]

[a] *Chair of Mechanical Process Engineering; Otto-von-Guericke-University Magdeburg*
[b] *The Laboratory of Fluid Dynamics and Technical Flows; Otto-von-Guericke-University Magdeburg*

Abstract

An experimental study is conducted on a pilot-scale zigzag air separator (ZZS) to study the effects of varying the solid feed mass stream, the mean channel air velocity, and the number of channel segments onto the grade efficiency. Spherical glass beads are classified. A straight pipe separator model (PSM) is modified for the ZZS and fitted to the experimental data to estimate the relative cut-point settling velocity, the separation sharpness, the relative rise velocity, the diffusion coefficient, and the particle loading. The proposed model is thoroughly investigated with regard to all important parameters, e.g. the estimated particle loading is shown to be more precise than the ratio of the solid and air mass stream, used in many publications. Finally, the relative rise velocity is shown to be only a function of the particle loading, making the experimental results within the model collapse.

Keywords: Classification, Model, Grade efficiency, Size distribution, Particle loading, Experiment

1. Introduction

A zigzag air separator (ZZS) is an apparatus for the separation of particulate materials into different fractions. The separator consists of an upright rectangu-

*Corresponding author. E-Mail: Berend.vanWachem@ogvu.de

lar channel with multiple sharp bends. Air is blown from the bottom to the top of the channel, while particles are fed about halfway upwards into the channel through a feed opening. The particle motion is driven by the interaction of gravity, fluid forces, as well as collisions with other particles and the walls of the apparatus. The aerodynamically light particles leave through the top of the channel, the so-called overflow outlet, and the aerodynamically heavy particles leave the channel through the bottom, the so-called underflow outlet.

The ZZS has a broad range of applications. It can be used to separate particulate materials based on different properties, such as size [1–3], density [4], and shape [5]. For instance, the ZZS is used for the separation and recycling of municipal waste [6], building rubble [4], shredded lithium-ion batteries [7] and thermoset composites [5].

For the characterization of the separation performance, grade efficiency curves are used. A grade efficiency curve describes the probability of fed particles with a specific set of properties to be carried out through the underflow. Particles with equal probability to be carried out to the overflow and underflow are referred to as cut-point particles. The separation sharpness indicates the gradient of the grade efficiency with respect to the particle properties around the cut-point.

Several publications [4, 6, 8] present experimental results and fit semi-empirical models to predict the separation process of the ZZS. The separation process in the ZZS depends on many different properties such as the separator geometry, e.g. the number, the bend angle, the depth, the width, and the length of the channel segments [6, 8], the composition of the separated material [6, 9, 10], as well as the operating process parameters, such as the air velocity in the channel, and the mass stream of feed material [3, 9, 10]. Despite the particle loading having a significant effect on grade efficiency, only a few authors have analysed its effect for their specific experimental setup [3, 9, 11, 12]. No good estimate of the particle loading for the separation with high feed mass stream is provided or incorporated in any of the current models.

To study the effects of different process parameters, including the particle loading, in this work an experimental study is conducted. In our experiments,

spherical glass beads are separated. The mean channel air velocity, the feed mass stream and the number of overflow segments are varied within these experiments. The resulting grade efficiencies are presented, analysed, and discussed.

The straight pipe separator model (PSM) published by Schubert et al. [13] will be adopted and applied to evaluate the experiments, as it provides a grade efficiency function and a residence time distribution for the separated particles. The mean particle residence time is used to estimate the particle loading during separation. Possibilities of data reduction by the dependency of the determined parameters are examined and discussed. To verify the model, the resulting differences between the experimental and modelled grade efficiency curves are compared. Furthermore, the model is validated by comparing the values and trends for the relative rise velocity and separation sharpness with results from the literature.

A brief review of the existing ZZS experimental data and modelling approaches is given in section 2. In section 3, the experimental setup of the pilot-scale ZZS, the characteristics of the separated glass beads and the investigated process parameter set are described. The observed particle movement patterns during separation and the derived semi-empirical model are described in section 4. The practical application of the derived model onto the experimental results is discussed in section 5. This includes the comparison of the shapes of the model and experimental grade efficiency curves as well as the effects of process parameter changes onto the separation sharpness, the cut-point, and the particle loading inside the channel. Furthermore, the direct relationship of the relative rise velocity with the particle loading is shown and discussed. The achieved results and possible applications of the model are concluded in the final section, 6.

2. Previous zigzag separator studies

Multiple authors have analysed the separation in the ZZS for various kinds of particulate materials. According to Kaiser [8], the main airflow in the ZZS forms a narrow band of high air velocity. The air moves from the bottom to

the top passing close to the protruding edges of the sharp bends in the channel. The air reaches a maximum velocity close to these protruding edges, while at the walls above the edges back-flow regions are formed. The particle movement is largely governed by this airflow pattern. Particles are transported upwards within the band of high air velocity. Particles that leave the main airflow in a channel segment accumulate at the downward sloping wall and slip along the wall, accelerated by gravity and back-flow down, to the lower protruding edge, where they either cross the main airflow region and fall to the next lower segment, or are captured by the upward airflow and transported into the channel segment above. Following this pattern, Kaiser considered the particles to be separated at each bend, which is considered to be a separation stage. Kaiser's model is based on a random walk model for the particles from stage to stage based on their property dependent probability to move upwards or downwards in each given stage. According to Kaiser, the overall grade efficiency of a ZZS with the same number of overflow and underflow channel segments and the total number of channel segments, z, is

$$T_{\mathrm{ZZS}} = \frac{1}{\left(1/T_1 - 1\right)^{z/2} + 1}, \tag{1}$$

with the single-stage grade efficiency T_1.

Senden [1, 6] studied an eight-and-a-half-segment ZZS with differing wall materials and channel widths between 51.8 mm and 141.4 mm. Also, the bend angle between the channel segments was varied with values of $90°, 120°$, and $150°$. The channel segment length and depth were kept constant with a value of 200 mm. Furthermore, the feed position was varied, feeding the particles directly below the first, the third, the fifth, or the seventh channel segment, counted from the bottom of the cascade. Differently sized square pieces of paper and spherical pieces of expanded polystyrene were separated. The paper pieces had an edge length of either 10 mm or 20 mm, a thickness of respectively 0.121 mm or 0.34 mm and a density of respectively $826\,\mathrm{kg/m^3}$ or $824\,\mathrm{kg/m^3}$. The expanded polystyrene pieces had a diameter of 4.5 mm and a density of $29\,\mathrm{kg/m^3}$. The mean channel air velocities ranged from $0.6\,\mathrm{m/s}$ to $3.9\,\mathrm{m/s}$. The separation

sharpness, as well as the residence time of the particles, varied with respect to the geometry, the separated particle type and the process parameters. The particle residence time ranged from 6.5 s to 55 s. The shortest residence time was observed for the 90° separator with a channel width of 141.4 mm separating the bigger paper squares, while the longest residence time was observed for the 51 mm wide separator with a bend angle of 150° and the smaller square-shaped particles. Senden presented a semi-empirical grade efficiency model for the ZZS, taking into account the different grade efficiencies for particles reaching a protruding edge either from below or above. This semi-empirical model was fitted to the experimental results and agreed well with the grade efficiency curves with low particle loadings for these low Stokes-number particles.

Vesilind and Henrikson [12] presented a study for the product purity and residence time of square plastic and aluminium particles with an edge length of 13 mm in an eleven-segment 120° ZZS. Unfortunately, the particle density and thickness were not reported in this publication. In the following study by Worrel and Vesilind [14] the length of a channel segment was given as 100 mm. Vesilind and Henrikson carried out separations with differing feed mass streams in the range from 1.1 g/s to 13.6 g/s while the mean channel air velocity was kept constant at 13.2 m/s. The particle concentration was measured over the height of the separator at each bend. For their experimental setup, Vesilind and Henrikson showed, that the maximum particle concentration is reached directly below the feed position, while the concentration decreases towards the underflow and overflow outlets. As expected, the particle loading in the channel increased with an increase in the feed mass stream. However, the mean residence time of the particles decreased with rising feed mass stream. The maximum mean residence time, $\tau_s \approx 130$ s, was estimated for a low feed mass stream of approximately 1.1 g/s, while for a high feed mass stream of approximately 9.2 g/s it decreased to $\tau_s \approx 95$ s. Furthermore, the probability for the particles to leave the separator through the underflow increased with increasing feed mass stream for both particle types, and therefore the cut-point shifted to aerodynamically lighter particles.

Rosenbrand [9] analysed the separation of rectangular foil particles in separators comparable to the 90° and 120° ZZS used by Senden, but for a higher feed mass stream, up to 4.8 g/s. The particle dimensions were given as 20 mm × 20 mm × 0.145 mm and 20 mm × 15 mm × 0.291 mm. The particle densities were 828 kg/m^3 and 825 kg/m^3, respectively. As in the work of Vesilind and Henrikson [12], an increase in feed mass stream caused an increase in the particle loading and a decrease in the particle residence time. However, differences were observed in the mean channel air velocity required to separate half of the feed material into the underflow and half into the overflow. The required air velocity increased in general for the 120° ZZS with rising feed mass stream. Hence, the effective cut-point settling velocity decreased, if not compensated by mean channel air velocity adjustment. This finding is consistent with the change in the cut-point settling velocity as described by Vesilind and Henrikson. However, for the 90° ZZS, an increase of feed mass stream caused either an increase or a decrease of the necessary air velocity based on other parameters, such as the separator wall material and the composition of the feed.

Biddulph and Connor [15] investigated the separation of binary mixtures of spherical polystyrene and polypropylene particles in a narrow ten- and six-segment ZZS with a bend angle of 115°, a channel depth of 190 mm, and width of 30 mm. The polypropylene particles had a density of 875 kg/m^3 and two different diameters, 4.763 mm and 7.94 mm. The polystyrene particles were different in size and density. The smaller polystyrene particles had a density of 987 kg/m^3 and a diameter of 6 mm. The bigger polystyrene particles had a density of 925 kg/m^3 and a diameter of 9.525 mm. The total length of the ten-segment ZZS was given as 2050 mm. The total length of the six-segment channel is not given directly and is estimated at 1230 mm, based on a sketch and the number of channel segments. The particles were separated with a mean channel air velocity range from 10 m/s up to 15 m/s. A diffusion-convection model was fitted to the separation of these binary mixtures to estimate the diffusion and convection terms. Biddulph and Connor proposed that the diffusion coefficient is a reciprocal value for the length utilisation of a separator for the separation

sharpness. Hence, separation in a separator of equal length and diffusion coefficients will show the same separation sharpness, while a decrease in length or an increase in diffusion coefficient will decrease the separation sharpness. Both ZZSs showed comparable diffusion coefficients, despite their different lengths, for a wide range of mean channel air velocities. The straight pipe separator generally showed a higher diffusion coefficient than the ZZSs. Furthermore, particles of different size and density showed different estimated diffusion coefficients in the straight pipe separator, which was not the case for these particles in the ZZS. Biddulph and Connor concluded that the zigzag arrangement reduced the wall-flow effects of particles, reducing the diffusion coefficient, especially for aerodynamically light particles.

Otto and Hartmann [16] proposed a hybrid model to describe the separation in the ZZS. The straight pipe separator model (PSM) from Schubert et al. [13] was combined with an artificial neuronal network. The network was trained to predict the parameters of the PSM for the separation with differing air temperature and humidity as well as to cope for electrostatic effects on the separation. Unfortunately, neither the experimental setup, the separation results, nor a qualitative assessment of the prediction quality was presented in detail.

Gillandt et al. [17] described the separation by size (classification) of glass beads in the diameter range of $0.1 - 1\,\mathrm{mm}$ with a solid density of approximately $2500\,\mathrm{kg/m^3}$ in a 13-segment ZZS. The bend angle was 120°. One single channel segment was 80 mm long, 40 mm wide, and had a depth of 42 mm. The air mass stream ranged from $4\,\mathrm{kg/h}$ up to $34\,\mathrm{kg/h}$, resulting in mean channel air velocities from $2.2\,\mathrm{m/s}$ up to $4.7\,\mathrm{m/s}$. The feed mass stream was varied up to $16.1\,\mathrm{g/s}$. The separations were evaluated for the cut-point diameter and the separation sharpness, based on the grade efficiency estimated from the particle size distributions of the underflow and overflow product. Also, the fluid velocity profile was measured by Laser-Doppler-Anemometry in two horizontal planes in the vertical direction for different channel air velocities. Furthermore, CFD-DEM simulations were carried out, to reproduce the experimental results. The

fluid simulation showed a good agreement with the measured time average of the air velocity profile. Despite this, the simulation predicted 25% higher cut-point diameters as observed in the experiments for low feed mass streams. Gillandt et al. observed different particle movement patterns in the separator. For low particle loadings, the particles moved bouncing back and forth between the channel walls and crossing the main airflow at other positions than the channel bends. For high particle loading, the glass beads moved in a vortex-like pattern. In each segment, particles rising with the main airflow and falling along the wall were seen, like in the pattern described by Kaiser [8]. Analogous to the results of Vesilind and Henrikson [12], Gillandt et al. found, that the cut-point diameter increases with increasing air velocity and an increase of feed mass stream cause a decrease in the cut-point diameter as well as in the separation sharpness.

Tomas and Gröger [10] presented a study on the separation with the ZZS by density with concrete-brick rubble and rubber granulates. The particle size was in the range from 4 mm up to 12 mm and the solid density from 1000 kg/m^3 up to 2800 kg/m^3. The particles were separated in a 16-segment ZZS with a channel width and depth of both 200 mm. The mean channel air velocity ranged from 7.5 m/s up to 14 m/s. The feed mass stream ranged from 33 g/s up to 175 g/s. Tomas and Gröger proposed a multi-segment separation model for the description of the total separator grade efficiency, based on the multi-segment model of Kaiser [8], adjusted for a differing number of overflow stages, z_O, and underflow stages, z_U, as well as differing single-stage grade efficiency functions for the overflow, T_O, and the underflow, T_U:

$$T_{\mathrm{ZZS}} = \frac{1}{1 + \dfrac{(1 - T_O)^{z_O}}{T_U^{z_U}}} \,. \tag{2}$$

The channel bend below the feed is counted as a separation stage for both the number of underflow stages and the number of overflow stages. The single-segment grade efficiency is based on the taping model proposed by Schubert [13], which was developed to describe the grade efficiency of rake and screw

classifiers. The single-segment separation function is given as:

$$T_O = T_U = \frac{1}{1 + \left(\frac{\dot{V}_f}{\dot{V}_s}\right)^{1 - \sqrt{\frac{\rho_s - \rho_f}{\rho_{s\,c} - \rho_f}}}}, \tag{3}$$

with the particle density, ρ_s, the cut-point density, $\rho_{s\,c}$, the air density ρ_f, the volume flow of air, $\dot{V}_f$, and mean volume flow of particles, $\dot{V}_s$. The model was fitted to the experimental data by adjusting the cut-point density and the a-priori unknown ratio of air and feed volume flow rate. The experimental and model grade efficiency curves showed good agreement after fitting. Even though the separated particles were distributed in size and shape, the separation evaluation according to the particle density showed a sharp separation. Therefore, this study showed that the ZZS is suitable for sharp density separation, even for complex particle mixtures.

Glöckner et al. [18] investigated the classification of sand with a size distribution ranging from 0.1 mm up to 1.2 mm, densities of approximately 2665 kg/m^3, and sphericities of approximately 0.89, in an eight-segment ZZS with a 120° bend angle and with a channel depth and width of 200 mm. The length of each channel segment was 400 mm. The mean air velocity varied in the range from 7.4 m/s up to 9.4 m/s. The particle loading was given as the ratio of feed mass stream to air mass stream, ranging from approximately 0.1 up to 1. The feed mass stream was published in the dissertation of Mann [2] for the same experimental series, ranging from 17.6 g/s up to 280.9 g/s. With an increase in mean channel air velocity, an increase of the cut-point diameter and a decrease in the separation sharpness was observed. With an increase in particle loading, the cut-point diameter, as well as the separation sharpness, decreased. The evaluation was conducted with the multi-segment separation model proposed by Tomas et al. [4]. The model gave a good representation of the experimental results after fitting.

Friedrich et al. [19] studied the classification of spherical glass beads in the size range from 0.8 mm up to 5 mm in a ten-segment zigzag channel with a chan-

nel width of 100 mm and a channel depth of 200 mm. Separation experiments and one-way coupled CFD-DEM simulations were carried out. The simulations were carried out with different RANS turbulence models, e.g. standard-k-ϵ, RNG-k-ϵ, and Menter-SST-k-ω. Despite the mean volumetric flux and the cut-point diameters were in close range of the experimental data, with differences less than 10%, all simulations yielded much sharper separations than observed in the experiment.

The above-presented studies cover a wide range of different separator geometries, feed material size, density and shape distributions, air velocities, as well as feed mass streams. Still, the experimental investigation of the parameter space given by the works discussed above is far from complete. Directly comparing existing studies is often not possible, as the evaluation methods and the measured parameters differ. Moreover, the distributions of particle size, shape, and density are not given in sufficient detail, or the separated particles do not have sufficient different classes to fit a model grade efficiency curve onto the experimental data. Also, no unifying model exists, presenting a good a-priori estimate of the cut-point and separation sharpness for any given combination of channel geometry, separated material, and process parameters.

3. Experimental setup

In this section, the experimental setup and the experimental procedure are described.

3.1. Test rig

The separation experiments are carried out in a pilot-scale ZZS test rig. The setup is sketched in Figure 1. The air in the test rig circulates in a closed-loop. The rotary blower (1) generates the differential pressure necessary for air circulation. From the blower, the air flows through the inflow pipe (2) before it enters the ZZS (3). Sensors in the inflow pipe measure the volumetric flow rate, the absolute pressure, the humidity, and the temperature of the airflow. The air flows from the ZZS through an aero cyclone (4) and a rag filter (5) before it

reaches the blower again. The feed material is stored in the silo (6) above the vibrating conveyor (7). The vibrating conveyor transports the particles to the feed chute, where they fall into the zigzag channel. The underflow product in the ZZS moves downwards into the underflow bin (8). Particles leaving the channel with the airflow as overflow product are separated from the airflow by the aero cyclone and are discharged into the overflow bin (9). Very small particles are separated from the airflow through the rag filter.

The zigzag channel is designed as a stack of modules, to enable the alteration of the geometry. The different modules are shown in Figure 2. From below, the zigzag channel starts with the bottom nozzle, Figure 2c, followed by a standard module, Figure 2a, and the feed module, Figure 2b. Up to two additional standard modules are stacked on top of the feed module, finalised by the top nozzle, Figure 2d. The three possible combinations of the modules are shown in Figure 3 and will be referred to as an eight-, six- or four-segment separator. Three sides of each module provide optical access. Only the right-hand-side wall and the feed chute are made of polyurethane-covered metal sheets.

The overflow length of the eight-, six- and four-segment separator are given as L_{O8}, L_{O6}, respectively, and L_{O4}, in Table 2. The underflow length, L_U, is constant and also given in Table 2.

The channel depth of the standard modules and the bottom nozzle is 200 mm. The top nozzle has a square cross-section, resulting in a linear depth decrease from 200 mm to 130 mm. The feed chute is aligned centrally within the ZZS and has a depth of 132 mm.

3.2. Glass beads

To analyse the separation by particle size, the particles have the same density, the same shape and a wide distribution in size. The particle size is subdivided into discrete diameter size classes. Each particle with diameter d belongs to the size class i if:

$$d_{\min i} \leq d < d_{\max i} \tag{4}$$

with the lower und upper size class borders, $d_{\min i}$ and $d_{\max i}$.

The particle size distribution (PSD) as volume-based frequency distribution is defined as

$$q_{3\,i} = \frac{V_{s\,i}}{(d_{\max i} - d_{\min i})\, V_s}\,, \tag{5}$$

with the total particle volume, V_s, and the volume of the particles within the ith size class, $V_{s\,i}$. The PSD is determined with a Camsizer from Retsch Technology GmbH. Fifty equidistant size classes in the range from 0 mm to 5 mm are used to evaluate the PSDs throughout the given work. An exemplary PSD for the glass beads is shown in Figure 4. The particle size distribution shows many clear peaks with gaps of low particle concentration due to the production process of the particles and the high resolution and precision of the measurement method. The low distance between the peaks of high particle concentration enables precise estimation of the grade efficiency in experiment. Also, the glass bead sphericity is measured with the Camsizer. It is defined as the ratio of the particle projection area and circle area of the circle with an equivalent circumference, $\Psi \geq 0.98$. Therefore, the particles are almost perfectly spherical. The particle density is specified by the manufacturer, $\rho_s = 2500\,\mathrm{kg/m^3}$.

The low spread in density and sphericity of the glass beads enables a good conversion of size classes into particle settling velocity classes. The wide diameter distribution of these glass beads enables a grade efficiency estimation within a wide range of classifier operation conditions.

3.3. Experimental procedure

The mean channel air velocity and the feed mass stream are controlled via the rotation frequency of the blower and the vibration intensity of the vibration conveyor, respectively. A higher rotation frequency of the blower results in a higher mean channel air velocity. A higher value of the vibration intensity results in a higher feed mass stream and, therefore, a higher particle loading.

There are also other parameters which influence the mean channel air velocity and the feed mass stream. The mean channel air velocity is also influenced by the pipe friction coefficient, which is influenced by the particle loading and the geometrical channel configuration, as well as by the density of the air. The

mass stream through the vibration conveyor is influenced by the temperature and humidity of the air and possibly by the particles, as these may change the electrostatic and friction forces between the particles. It is observed that the layer thickness of transported particles on the conveyor bed changes between experiments, even for separations with equal vibration intensity. This causes mass stream differences between experiments of up to 30%.

Based on preliminary experiments with the eight-segment separator, a parameter set of six vibration intensities and five rotation frequencies are established to distribute the resulting cut-point diameter, while varying the feed mass stream and the mean channel air velocity. Considering the three different geometries, this results in a total of 90 separation experiments. However, for some settings, the experiments were not fruitful, and finally, a total of 83 experiments were evaluated.

The feed time, t_f, is set to achieve enough particles in the overflow and underflow products to enable an evaluation of the grade efficiency. The resulting parameter range for the fluid density, ρ_f, the mean channel air velocity, u, the feed mass stream, $\dot{m}$, the total feed material mass, m_f, and the recovery of the underflow product, R_U, are given in Table 3 for all evaluated experiments. Each of the experiments is carried out batch-wise, where after setting the correct control variables of the ZZS, the measurements and the feed are started. The separation products are scaled, reduced to feasible sample size, and analysed via the Camsizer.

4. Separation model

In this section, the modification and application of the PSM published by Schubert et al. [13] are described in detail. The fluid and particle movement patterns in the ZZS are presented in section 4.1. The adaptation of the PSM is described in section 4.2. The estimation of the experimental grade efficiency values based on the experimental results is described in section 4.3. The fit of the model to the experimental results is described in section 4.4. In section 4.5, the derivation of the additional separation parameters important for model

validation e.g. the cut-point settling velocity, the separation sharpness, and the particle loading, is described. The dimensionless cut-point settling velocity and the dimensionless rise velocity are discussed in section 4.6.

4.1. Particle movement pattern

The particle movement inside the separator is complex and three-dimensional. It is governed by particle-fluid, particle-wall, and particle-particle interactions. Many patterns can be recognised in the stochastic particle movement, as was shown by Roloff et al. [20], who measured and analysed the two-dimensional particle velocity distribution of glass beads during the separation in the bends of an eight-segment zigzag air separator. The more movement patterns are distinguished, the more ambiguous is the assignment of a given particle trajectory to one of these patterns. Furthermore, the influence of the individual patterns on the separation function is more difficult to determine. Therefore, only the two most important particle movement patterns are used as the basis for the modelling and explained in detail below. Despite the differences in the observed particle movement patterns, the airflow structure is similar in all studies [6, 8, 9, 11, 17], as described in section 2. The flow and particle movement patterns are illustrated in Figure 5.

The first particle movement pattern, (a), is a stochastic bouncing of the particles through the channel. It is described by Gillandt et al. [17] and is illustrated in Figure 5a. The particles bounce back and forth between the channel walls, crossing the main airflow regularly. This leads to a regular momentum exchange between the fluid and the particles. The full length of the zigzag channel is utilized for the separation of the particles.

In the second pattern, the particles move in a vortex pattern in each channel segment, see Kaiser [8], Tomas et al. [4], and Glöckner et al. [18]. This particle vortex pattern is described by Senden [6] as a superposition of two independent movement patterns.

The first sub-pattern, (b), is illustrated in Figure 5b. The particles slide down along the inclined lower wall of a segment, accelerated by gravity and the

lack of an upward-directed flow. A particle builds up a downwards directed velocity before it reaches the channel bend. Here, it is exposed to the main airflow and is separated. Either the downward directed momentum of the particle is eliminated by the fluid drag of the rising airflow and the particle is captured by the rising airflow, or the particle crosses the main airflow reaching the downwards inclined wall of the lower segment at the opposite side. In the first case, the particle starts to rise according to the second movement sub-pattern, (c), described below. In the second case, it will move further downwards according to this movement pattern, (b), along the inclined wall, reaching the next lower protruding edge.

The second sub-pattern (c) is illustrated in Figure 5c. The particles are carried upwards by the airflow within the main airflow until they either leave the main airflow or the separator through the overflow outlet. There are several causes for a particle to leave the main airflow. The main airflow follows the inclined channel segments. The mean drag force on a particle is therefore also inclined, while the gravity pulls it downwards. This difference in direction may pull particles out of the airflow towards the lower channel wall. Additionally, the main airflow follows a channel bend, while particles tend to move straight and are ejected, due to their inertia. Furthermore, particles crossing the main airflow according to the pattern (b) can knock rising particles out of the airflow due to collisions. Therefore, particles are mostly ejected from the main airflow towards the inclined wall below, where they start to move according to the pattern (b) in the current segment.

Particles which follow patterns (b) or (c) show a difference in local particle residence time and differ in their probability to move upward or downward when they reach a channel bend, as was shown by Senden [6] and Rosenbrand [9].

Gillandt et al. [17] recognised a transition in the particle movement from stochastic movement according to pattern (a) to the formation of particle vortexes with increasing feed mass stream. Therefore, the particle movement inside the ZZS can be seen as a superposition of all three particle movement patterns, with an increasing influence of the patterns (b) and (c) due to increasing particle

loading.

This change in pattern is also observed for separations carried out in this work. For low feed mass streams, the pattern (a) as shown in Figure 5a is confirmed for all three geometries. For low feed mass streams, the general particle concentration is low. The particles are distributed evenly, without the formation of regions with high concentration. The transition in the particle movement pattern from the stochastic bouncing through the channel to the formation of particle vortexes is observed after the feed mass stream is increased. With increasing feed mass stream, dense downwards directed particle streams are formed at the protruding edges, directed into the main airflow as shown in Figure 5b for the pattern (b). These streams are clearly visible, having a higher opacity than the surroundings, indicating high local particle concentrations. Never the less, all carried out experiments show particles moving according to the pattern (a). Even for the eight-segment experiments with the highest feed mass stream, particles are observed bouncing back and forth in the channel at other positions than the bends. Therefore, the gradual change in movement pattern as described by Gillandt et al. [17] is confirmed.

4.2. Straight pipe separator model

Gillandt et al. [17] showed that glass beads at low particle loadings move according to the pattern (a). This pattern contradicts a multi-stage modelling approach, as the particles move in a stochastic fashion through the channel, crossing the main airflow regularly independently from the channel bends. This movement is similar to the particle behaviour in a straight pipe air separator, where the particles also move back and forth due to particle-fluid, particle-wall, and particle-particle interactions.

A semi-empirical modelling approach for the straight pipe separator is given by Molerus and Hoffman [21]. The particle transport is modelled as a convection and diffusion process in steady-state, based on the Fokker-Planck-equation,

$$\frac{\partial r}{\partial t} = -\frac{\partial}{\partial x}\left(v_a\, r\right) + \frac{\partial^2}{\partial x^2}\left(D\, r\right) \tag{6}$$

with the particle concentration, r, the time, t, the spatial coordinate, x, the convection term, v_a, and the diffusion term, D. The particle convection describes the mean velocity of a particle with specific properties. The diffusion coefficient describes how fast particles are transported from regions of high particle concentration to regions of low particle concentration due to their stochastic movement. The diffusion coefficient is assumed to be constant for a given separation. The convection term is assumed to be

$$v_a = v_0 - v_t \tag{7}$$

with the particle rise velocity, v_0, and the terminal particle settling velocity, v_t. The particle rise velocity is assumed to be constant for all particles during a separation.

The particle rise velocity, v_0, and the diffusion coefficient, D, were used successfully as fitting coefficients by Molerus and Hoffmann [21], to fit the model grade efficiency curves to the experimental results of straight pipe separators. Nevertheless, Molerus and Hoffmann use rather arbitrary assumptions for the boundary conditions in their model. The particle discharge at the overflow is assumed to be the product of the particle concentration at the overflow and the particle rise velocity, v_0. The particle discharge at the underflow is assumed to be the product of the particle concentration at the underflow and the particle settling velocity, v_t. This causes the particle discharge to be dependent on the particle properties at the underflow, and not at the overflow.

The model of Schubert et al. [13] is a solution to the Fokker-Planck equation (6), where the particle concentration is the variable parameter, and the overflow and underflow mass fluxes are the boundary conditions at the top and bottom of the classifier, respectively. However, with the current experimental setup, the exact particle concentrations at the under- and overflow are not known. Therefore, the assumption that all particles reaching an outlet will be immediately

discharged without back-mixing will be used. The resulting grade efficiency [13]

$$T_{\mathrm{PSM}}\left(v_t, v_0, D, L_O, L_U\right) = \frac{1}{1 + \dfrac{\exp\left(\dfrac{v_0 - v_t}{D} L_U\right) - 1}{1 - \exp\left(-\dfrac{v_0 - v_t}{D} L_O\right)}} \tag{8}$$

depends on the overflow channel length, L_O, the underflow channel length, L_U, the diffusion coefficient, D, the particle rise velocity, v_0, and the particle settling velocity, v_t. The grade efficiency for the particle without convection, thus $v_0 = v_t$, is given as

$$T_{v_0} = \frac{1}{1 + \dfrac{L_U}{L_O}}, \tag{9}$$

resulting in the rise velocity grade efficiencies, $T_{v_0 4} = 0.127$, $T_{v_0 6} = 0.418$, and $T_{v_0 8} = 0.564$.

For the calculation of the terminal settling velocity, the buoyancy is neglected. Therefore, the terminal settling velocity is:

$$v_t = \sqrt{\frac{4}{3} \frac{g\, \rho_s\, d}{\rho_f\, c_D}}\ , \tag{10}$$

with the particle diameter, d, the drag coefficient, c_D, the gravitational acceleration, $g = 9.81\,\mathrm{m/s^2}$, the particle density, ρ_s, and the air density, ρ_f.

All particles are assumed to be separated in the Newton-regime. The drag coefficient is thus assumed to be

$$c_D = 0.44\,. \tag{11}$$

4.3. Experimental grade efficiency

To enable the fit of the PSM, equation (8), the experimental grade efficiencies have to be determined for each experiment. They are determined from the settling velocity, $v_{t\,i}$, and the grade efficiency, T_i, for each size class, i. The mean diameter,

$$d_i = \frac{d_{\min\,i} + d_{\max\,i}}{2} \tag{12}$$

is converted to the corresponding class settling velocity, $v_{t\,i}$, by equation (10). As the fluid density may change, it is estimated for each experiment separately.

Therefore, the settling velocity for a given size class may differ between experiments.

The determination of the grade efficiency values, T_i, based on product masses and PSDs, can be found in the relevant technical literature [22]. The grade efficiency

$$T_i = R_U \frac{q_{3\,U\,i}}{q_{3\,F\,i}} \tag{13}$$

is a function of the frequency size distribution for the underflow product, $q_{3\,U\,i}$, the frequency size distribution of the feed material, $q_{3\,F\,i}$, as well as the underflow recovery, R_U. The underflow recovery is given as,

$$R_U = \frac{m_U}{m_F} \tag{14}$$

with the underflow product mass, m_U, and the feed material mass, m_F. It is assumed, that all particles entering the separator through the feed are discharged into one of the products. Therefore, the feed material mass

$$m_F = m_U + m_O \tag{15}$$

is the sum of the underflow and overflow product mass. The feed PSD is given as

$$q_{3\,F\,i} = R_O\, q_{3\,O\,i} + R_U\, q_{3\,U\,i} \tag{16}$$

with the overflow recovery, R_O and the underflow recovery, R_U.

4.4. Model fit

The PSM, given by equation (8), is fitted to the experimental results by adjusting the particle rise velocity, v_0, and the diffusion coefficient, D, to minimize the weighted RMSE

$$\begin{aligned} F = \min_{v_0,\, D} & \sqrt{\sum_i \left(T_{\mathrm{PSM}}\left(v_{t\,i}, v_0, D, L_O, L_U\right) - T_i\right)^2 w_i} \\ s.t.\, & v_0 > 0 \\ & D > 0\ , \end{aligned} \tag{17}$$

with the weighting coefficients, w_i, and the discrete experimental grade efficiencies, T_i, while the particle rise velocity and the diffusion coefficient have to be

positive. The underflow and overflow lengths, L_U and L_O, are taken from the ZZS geometry and are given in Table 2.

As can be seen from Figure 4, the PSD has a non-uniform distribution. This leads to a statistical scatter in the experimental grade efficiency for size classes with a low number of separated particles. To reduce the scatter influence onto the fit, weighting coefficients are introduced. A reliable fit with the given experimental data is achieved with the weighting coefficients

$$w_i = \frac{q_{3\,F\,i}^2}{\sum\limits_j q_{3\,F\,j}^2}\,, \tag{18}$$

based on the PSD of the feed material, $q_{3\,F\,i}$.

4.5. Derivation of particle loading, cut-point settling velocity, and separation sharpness

The particle loading, s, the particle hold-up, m_s, the mean particle residence time, τ_s, the cut-point settling velocity, v_c, and the separation sharpness, κ, can be obtained from the fitted grade efficiency parameters and the measured process parameters. The cut-point settling velocity and the separation sharpness are a widely used concept to describe the position and shape of the grade efficiency. The particle hold-up and the particle loading influence the particle-particle and particle-fluid interactions in the channel.

Schubert et al. [13] provide the particle residence time distribution as

$$\tau = \frac{1}{v_0 - v_t}\left(\left(1 - T_{\mathrm{PSM}}\right) L_O - T_{\mathrm{PSM}} L_U\right) \tag{19}$$

with the terminal settling velocity, v_t, and the fitted PSM parameters, as described by equation (8). The total particle hold-up, m_s, is given as

$$m_s = \sum_i \tau_i\, \dot{m}_{F\,i}\,, \tag{20}$$

with the feed mass stream, $\dot{m}_i$, and the residence time, τ_i, for each size class, i. The feed mass stream fraction is estimated as

$$\dot{m}_{F\,i} = \frac{m_F}{t_f} q_{3\,F\,i}\left(d_{\max\,i} - d_{\min\,i}\right) \tag{21}$$

with the PSD of the feed, $q_{3\,F\,i}$, the total mass of feed particles, m_F, the upper and lower diameter borders, $d_{\max i}$ and $d_{\min i}$, as well as the duration of experimental particle feed, t_f.

The particle loading

$$s = \frac{m_s}{m_f} \tag{22}$$

inside the channel, is given by the fraction of the particle hold-up, m_s, and the mass of air inside of the channel, m_{air}. The air mass is calculated as

$$m_f = A\,(L_O + L_U)\,\rho_f\,, \tag{23}$$

based on the channel cross-section area, A, the overflow and underflow lengths, L_O and L_U, and the fluid density, ρ_f.

The mean particle residence time is defined as

$$\tau_s = \frac{m_s}{\dot{m}_F}\,, \tag{24}$$

with the hold-up, m_s, and the mean feed mass stream, $\dot{m}_F$.

To compare the experiments with each other and with the literature data, the cut-point settling velocity, v_c, and the separation sharpness, $\kappa_{25\,75}$, are used. The cut-point is defined as the particle with 50% probability to be carried out in underflow and overflow, $v_c = v_{t\,50}$. The separation sharpness is defined as

$$\kappa_{25\,75} = \frac{v_{t\,25}}{v_{t\,75}}\,, \tag{25}$$

with the settling velocity values, $v_{t\,25}$ and $v_{t\,75}$, for which 25% and 75% of the particles are separated through the underflow outlet.

Some authors evaluate the separation sharpness based on the particle diameter [3, 11, 17]. The conversion of the separation sharpness between size and settling velocity is

$$\kappa_{d\,25\,75} = \frac{d_{25}}{d_{75}} = \frac{v_{t\,25}^2}{v_{t\,75}^2} = \kappa_{25\,75}^2\,, \tag{26}$$

as given by equation (10).

4.6. Relative rise and cut-point settling velocity

The relative rise velocity and the cut-point settling velocity are two distinctive velocities describing points of the grade efficiency. The rise velocity is defined by the PSM, given by equation (7) and (8) as the settling velocity of the particle without convective transport. The grade efficiency value is given by equation (9). While the cut-point gives the particle settling velocity of the particle with equal probability to be carried out through the overflow and the underflow. Both values are identical for a symmetrical separator with equal overflow and underflow lengths, $L_O = L_U$.

The PSM, given by the equations (7), (8), (10), and (11), presuppose a linear relationship between the rise velocity and the mean channel air velocity. Furthermore, the rise velocity is supposed to be independent of the number of overflow and underflow segments. Therefore, the relative rise velocity is defined as

$$v_{0\,n} = \frac{v_0}{u}, \tag{27}$$

with the rise velocity, v_0, and the mean channel air velocity, u. If these considerations are confirmed by experiments, it would reduce the complexity of the separation model, as the rise velocity would be solely a function of the particle loading. Also, the relative cut-point settling velocity, defined as

$$v_{c\,n} = \frac{v_c}{u}\,, \tag{28}$$

should enable a better comparison of different feed mass streams and separator geometries, as it is considered to be independent of the mean channel air velocity.

5. Results and discussion

First, one single separation experiment is discussed in detail, to illustrate the applied techniques for fitting and evaluation in section 5.1. The direct effects of the conveyor settings, the blower settings and the change in the number of channel segments onto the experimental and fitted grade efficiencies for a representative subset of experiments are discussed in section 5.2. The results

for all 83 separation experiments are discussed in the subsequent subsections. The mean particle residence time and particle loading are shown and discussed in section 5.3. The influence of the particle loading on the relative cut-point settling velocity is discussed in section 5.4, on the separation sharpness in section 5.5, and on the relative rise velocity in section 5.6.

5.1. Single separation evaluation

In this section, one separation with an eight-segment ZZS is presented in detail. The given experiment has a low feed mass stream and a medium mean channel air velocity, separating the feed material into nearly equal product mass fractions, $R_U = 0.496$. The process parameters and results for this separation are summarized in Table 5 and illustrated in Figure 6. The PSDs for the underflow and overflow products are presented in Figure 6a, normalised by their respective recoveries and stacked on each other. Therefore, the feed mass split for each size fraction is illustrated according to equation (16).

The following quantities are illustrated in Figure 6b: the calculated settling velocity classes, $v_{t\,i}$, given by equation (10), the resulting experimental grade efficiencies, T_i, given by equation (13) and the fitted PSM, T_{PSM}, given by equation (8). The marker-area of the data-points in Figure 6b is proportional to their corresponding weighting coefficient, w_i. As can be seen, the PSM fits very well to the experimental grade efficiency points with high weighting coefficients. This is also confirmed by the very low weighted RMSE, $F = 0.0058$. Therefore, the PSM provides a suitably shaped grade efficiency to describe the experimental data.

The cut-point diameter, d_c, determined from the cut-point settling velocity, v_c, agrees well with the feed mass split shown in Figure 6a. Furthermore, the found separation sharpness, $\kappa_{d\,25\,75} = 0.88$, agrees well with the experimental results presented by Gillandt et al. [17] for a twelve-segment separator with a low particle loading, $\kappa_{d\,25\,75} = 0.9$. It can be concluded that the used evaluation method produces coherent results for the cut-point and the separation sharpness.

5.2. Comparison of conveyor setting, blower setting and segment number effects on the grade efficiency

The controlled variables, the number of channel segments, the vibration intensity of the conveyor, and rotation frequency of the blower, have a direct influence on the resulting process variables and grade efficiency. The feed mass stream and the mean channel air velocity vary according to the controlled variables and measured variables as described in section 3.3. The direct effects of the controlled variables on grade efficiency can be seen in Figure 7. In Figure 7a the number of segments, in Figure 7b the vibration intensity of the conveyor, and in Figure 7c the rotation frequency of the blower are varied, while the other controlled variables remain unchanged.

Increasing the number of overflow segments decreases the cut-point settling velocity and increases the separation sharpness. Increasing the feed mass stream decreases the cut-point settling velocity as well as the separation sharpness. An increase in mean channel air velocity increases the cut-point settling velocity, while no change in separation sharpness is observed.

All PSM grade efficiency curves shown in Figure 7 fit well to the experimental results, except the four-segment separator curve shown in Figure 7a. The experimental and the PSM grade efficiency for the four-segment separator are asymmetric s-shaped curves, as can be seen in the figure. The experimental grade efficiency shows a larger curvature before the cut-point, $T_{\mathrm{PSM}} = 0.5$, compared to after the cut-point. This is even more pronounced in the fit of the model. This reduces the quality of the fit. The model does not accurately describe the underlying separation behaviour of the four-segment separator.

The difference between the PSM and the four-segment separation results are caused by particle movement patterns which are not considered in the model. The model assumes a convective and diffusive transport only, with constant properties over the whole length of the ZZS. The model predicts a high particle discharge probability through the overflow, even for fast settling particles, due to the short overflow length. In the experiments, other particle movement patterns resulting from geometrical features of the channel are observed. The particles

enter the channel from the feed chute inclined downwards. This increases effectively the overflow length, as the entering particles first lose altitude before they reach a steady-state motion according to the convective and diffusive transport. Additionally, many particles hit the inclined walls of the top nozzle, by which they are deflected into the channel. These perturbations of the local particle movement pattern are present in all geometrical configurations. But, they only change the grade efficiency of the four-segment separator significantly, as the short overflow length can not compensate for these local effects.

Never the less, the difference between the PSM and the experimental grade efficiency is generally small, as can be seen from the RMSE, $F = 0.021$, for the four-segment separation shown in Figure 7a and the highest overall RMSE, $F = 0.044$, within all four-segment separations. The grade efficiencies for the eight- and six-segment separators align better, with a smaller maximum RMSE, $F = 0.028$, which confirms the applicability of the PSM.

5.3. Mean particle residence time and particle loading

The particle loading in the ZZS has a direct influence on the grade efficiency. In practical applications, there is usually no reliable way to estimate the particle loading during separation. Therefore, the ratio of feed mass stream by air mass stream is used as a substitute [2, 3, 10, 18]. This method of estimating the particle loading does not account for the difference in residence time between the particles and the fluid, for which the ratio can take values of 10 up to 40, as in the work of Rosenbrand [9] or more than 100 as in the work of Vesilind and Henrikson [12]. Therefore, the estimate of the particle loading can be wrong by more than two orders of magnitude. Furthermore, the residence time of the particles depends on the particle properties and process parameters.

In the current work, the mean particle residence time and the particle loading are estimated, as described in section 4.5. The derived order of magnitude for the particle residence time, τ_s, is confirmed by the human eye and a stopwatch during the separation experiments. The results of the model for particle loading and residence time are presented and discussed in this section.

In Figure 8a, the mean particle residence time is shown as a function of the underflow recovery. It can be seen from the figure, that the recovery, R_U, has a significant influence on the mean particle residence time. It is a measure for the minimum distance a specific particle fraction has to travel for ejection. For the four-segment separator low values of underflow recovery result in a low particle residence time, as most particles are ejected through the very short overflow. Furthermore, particles with settling velocities close to the rise velocity, have a small convection velocity. They have a longer residence time and contribute stronger to the particle loading. Therefore, the mean particle residence time increases for separations with recoveries of $R_U \approx 0.5$, as the rise velocity lies centrally in the settling velocity distribution of the glass beads, resulting in more particle size classes with high residence time. These effects are covered by equation (24) of the PSM.

The particle loading is shown as a function of the mean feed mass stream in Figure 8b. For the eight- and six-segment separator, the particle loadings overlap very well with each other, indicating that an increase in the separator length will cause an equivalent increase in the particle hold-up, so the classifier volume and the residence time increase proportionally.

For the eight- and six-segment separator, the particle loading increases with the feed mass stream. The slope of these curves decreases slightly with rising feed mass stream, indicating a mean particle residence decrease for higher particle loadings. This effect was also observed by Vesilind and Henrikson [12] and Rosenbrand [9].

As observed before, the behaviour of the four-segment separator differs from the longer geometries. As can be seen from Figure 8b, the calculated particle loading shows a high scatter with a generally low particle loading. Due to the shorter overflow length of the four-segment separator, particles leave the ZZS much faster through the overflow as they leave through the underflow. Therefore, their contribution to the hold-up is much smaller and the residence time decreases significantly with increasing rise velocity. This can also be seen from the very low mean residence times, $\tau_s < 0.2\,\mathrm{s}$, for the separations where

only a small part of the feed material is ejected through the underflow outlet, $R_U < 0.15$.

5.4. Relative cut-point settling velocity

In this subsection, the relative cut-point settling velocity is compared for all separation experiments as a function of the particle loading and number of channel segments. In Figure 9, the relative cut-point settling velocity as a function of the particle loading, for the four-, six- and eight-segment separator is shown. For each geometrical configuration, the experimental points align well, showing a general trend with low scatter. As expected, the relative cut-point settling velocity is higher for separations with a short overflow, hence the four-segment separator has the highest relative cut-point settling velocity, while the eight-segment separator has the lowest.

The mean channel air velocity has no significant influence on the relative cut-point settling velocity. The effect of the mean channel air velocity is thus completely accounted for, by the division of the cut-point settling velocity with the mean channel air velocity.

An increase in particle loading decreases the relative cut-point settling velocity, as expected. The particle loading estimated by equation (22) is suitable to collapse the relative cut-point settling velocity onto one line for each geometrical configuration, as can be seen in figure Figure 9. This line has a change in slope with increasing particle loading. To approximate this change, two linear functions are combined as:

$$v_n = \begin{cases} as + b, & \text{if } s \leq 0.4 \\ cs + 0.4\,(a - c) + b, & \text{otherwise} \end{cases} \tag{29}$$

with the coefficients a, b, and c. The position of the function bend is set to $s = 0.4$, as a more precise position can not be estimated, due to the lack of experimental values within this particle loading region. a and c define the slope of the first and the second section of the function, respectively, while b gives the intersection of the function with the ordinate. The function is fitted to

the cut-point settling velocities for each geometrical configuration, as shown in Figure 9. The resulting coefficients and RMSE are given in Table 6. The initial slope is more than two times more negative than the slope of the second section of the function for each geometrical configuration.

5.5. Separation sharpness and diffusion coefficient

As the separation sharpness and the diffusion coefficients of the four-segment separator show a high deviation due to the difference in experimental and model grade efficiency, only the six- and eight-segment separation results will be discussed in this section.

In Figure 10b the diffusion coefficient for the six- and eight-segment separator are shown as a function of the particle loading. For the separations with low particle loading, $s < 0.2$, the diffusion coefficients are similar. They rise from $D \approx 0.5\,\mathrm{m/s^2}$ to $D \approx 0.57\,\mathrm{m/s^2}$, as particle loading increases. For higher particle loadings, the six-segment separator shows no further increase in the diffusion coefficient, while the diffusion coefficient for the eight-segment separator rises further with increasing particle loading. A higher mean channel air velocity also results in a slightly larger diffusion coefficient.

In Figure 10a the separation sharpness for the six- and eight-segment separator is shown as a function of the particle loading. The eight-segment separator shows a higher separation sharpness than the six-segment separator. The separation sharpness decreases with an increase in particle loading. The decrease is non-linear, with a faster descent for low particle loadings. The clear trends observed in the separation sharpness of the eight- and six-segment separator confirm the dependency of the separation sharpness to the particle loading. The low scatter for these values confirms the independence from the mean channel air velocity. Therefore, the separation sharpness is more suitable to describe the change in the grade efficiency than the diffusion coefficient, as it depends on the particle loading only.

5.6. Relative rise velocity

Figure 11 shows the relative rise velocity for the four-, six- and eight-segment separator as a function of the particle loading. The trends for the relative rise velocity show a fast decrease with particle loading for low particle loadings and a slower decrease for higher particle loadings. This is similar to the relative cut-point settling velocity functions presented and discussed in section 5.4. Therefore, the segmented function consisting of two linear parts given by equation (29) is fitted to the relative rise velocity for each geometrical configuration. The functions are shown in Figure 11. The coefficients and RMSE are presented in Table 7.

All three curves show only small deviations from each other and a low spread. The difference between the maximum and the minimum relative rise velocity for any given particle loading is less than 10%. This confirms the following assumptions, described in the modelling section 4:

- The relative rise velocity is independent of the number of overflow segments.
- The relative rise velocity is independent of the mean channel air velocity. Hence, the rise velocity is proportional to the mean channel air velocity.
- A constant drag coefficient for the calculation of the settling velocity of the spherical particles is appropriate.
- The particle loading estimated by equation (22) is a measure for the change in the particle movement characteristics.

The relative rise velocity is high, $1.82 < v_{0\,n\,\max} < 2.0$, for a very low particle loading, $s < 0.04$. A comparably slow fluid transports particles with an up to two times higher settling velocity upwards in an inclined channel. There are several reasons for this phenomenon. The airflow forms a band of high air velocity in the centre of the channel with a maximum air velocity of more than two times the mean channel air velocity [17, 23]. Furthermore, the airflow is turbulent, which may cause the effective drag coefficient to rise [24].

Additionally, the particles are moving back and forth in the channel, increasing their relative velocity with the fluid and, therefore, increasing the drag force acting on them in the channel direction. The magnitude of the relative rise velocity is also confirmed by the experimental data published by Gillandt et al. [17] for the separation of glass beads up to 1 mm in size and for low particle loadings in a twelve-segment separator. Based on the published values for the cut-point diameter and the mean channel air velocity, the rise velocity range is estimated as $1.41 < v_{0\,n\,\max} < 1.89$. This matches the rise velocity values shown in Figure 11.

With increasing particle loading, the relative rise velocity decreases. This is due to the change in particle movement pattern, as described in section 4.1, resulting in a shorter exposition of single particles to the main airflow. Additionally, it can be assumed that the fluid velocity profile changes. Kussin and Sommerfeld [25] showed that an increase in particle loading in a confined turbulent flow may dampen the turbulence effects and widen the fluid flow profile. This decreases the maximum air velocity and reduces the turbulence effect on the resulting drag coefficient for the particles, decreasing the rise velocity.

6. Conclusions

An experimental campaign studying the separation of glass beads in a zigzag air classifier with a total of 83 evaluated separation experiments is carried out and presented. The influences of feed mass stream, mean channel air velocity and the number of overflow channel segments are studied. The relative cut-point settling velocity, the cut-point diameter, the separation sharpness, the relative rise velocity and the diffusion coefficient are derived, based on an adapted straight pipe separator model (PSM).

The effects of the controlled variables can be summarized as follows. An increase in feed mass stream increases the particle loading. An increase in particle loading decreases the separation sharpness, the relative cut-point settling velocity, and the relative rise velocity, while it increases the diffusion coefficient. Hence, even smaller particles leave the separator through the underflow outlet

and the general quality of the separation is reduced. For the six- and eight-segment separator an increase in particle loading decreases the residence time of the particles. An increase in mean channel air velocity increases the diffusion coefficient, while no effects on the separation sharpness and the relative cut-point settling velocity are observed. Furthermore, an increase in the number of overflow segments increases the separation sharpness and the residence time of the particles, while it decreases the relative cut-point settling velocity.

The applied straight pipe separator model fits very well to the six- and eight-segment experimental grade efficiencies, while a small shape mismatch to the experimental four-segment grade efficiency is observed.

The overflow and underflow length, the rise velocity, and the diffusion coefficient fully describe the shape of the grade efficiency curve of the PSM. The overflow and underflow lengths are given by the geometry. The rise velocity describes a specific point of the grade efficiency according to equation (9). It is shown, that the rise velocity is a function of the particle loading. Furthermore, the rise velocity is directly proportional to the mean channel air velocity and is independent of the number of channel segments. Therefore, the found characteristic for the relative rise velocity describes well the change of the grade efficiency. However, the diffusion coefficient shows non-linear dependencies on the particle loading, which are not present in the model itself. The effect of separation sharpness on the difference between rise velocity and cut-point settling velocity is small, for rather symmetrical ZZS configurations, e.g. the six- and eight-segment configuration presented. Hence, a good prediction of the cut-point by the model is achieved.

Acknowledgements

This work is part of the German priority program (SPP) 1679 that is financially supported by the Deutsche Forschungsgemeinschaft (DFG), Germany.

Acronyms

CFD	Computational fluid dynamics.
DEM	Discrete element method.
PSD	Particle size distribution.
PSM	Simplified straight pipe separator model from [13] with the grade efficiency according to equation (8).
RMSE	Root mean square error of the PSM grade efficiency to the experimental results.
ZZS	Zigzag air separator.

Symbols

A	Cross-section area of the zigzag air separator in m^2.
c_D	Drag coefficient.
d	Particle diameter in mm.
D	Turbulent diffusion coefficient as defined by Schubert et al. [13] in $\frac{\mathrm{m}^2}{\mathrm{s}}$.
F	Target function of the minimization according to the root mean square error between the experimental and model grade efficiency.
g	Gravitational acceleration, 9.81 $\frac{\mathrm{m}}{\mathrm{s}^2}$.
H	Height of an element in mm.
L	Length of an element in mm.
m	Mass in kg.
$\dot{m}$	Mass stream in $\frac{\mathrm{g}}{\mathrm{s}}$.
q	Volume-based particle size distribution (PSD) in $\frac{\%}{\mathrm{mm}}$.
r	Particle number per unit volume in $\frac{1}{\mathrm{m}^3}$.
R	Recovery as the ratio between a given product mass and the feed mass.
s	Particle loading as the ratio between the particle mass and air mass in the separator.
t_f	Feed duration in s.
T	Grade efficiency.
u	Mean channel air velocity in $\frac{\mathrm{m}}{\mathrm{s}}$.
v	Particle velocity in $\frac{\mathrm{m}}{\mathrm{s}}$.
V	Volume in m^3.
$\dot{V}$	Volumetric flow rate in $\frac{\mathrm{m}^3}{\mathrm{s}}$.
w	Weighting coefficient in m^2.
W	Width of an element in mm.
x	Height coordinate in m.
z	Number of separation stages.
κ	Separation sharpness.

φ	Bend angle between channel segments of the ZZS in degree.	ρ	Density in $\frac{\mathrm{kg}}{\mathrm{m}^3}$.
Ψ	Particle sphericity coefficient.	τ	Particle residence time in s.

Subscripts

		F	Feed.
0	Convection free particle.	i	Iteration variable used for size and velocity classes.
1	Single-segment.		
3	Volume or mass-based estimation.	j	Iteration variable used for size and velocity classes.
25	Twenty fifth percentile.	**max**	Maximum value.
75	Seventy fifth percentile.	**min**	Minimum value.
a	Absolute value.	n	Normalised value.
B	Bottom nozzle.	O	Overflow.
c	Cut-point particle.	s	Solid.
C	Feed chute.	t	Terminal settling.
e	Experimental result.	T	Top nozzle.
f	Fluid.	U	Underflow.

References

[1] M. Senden, Performance of zigzag air classifiers at low particle concentrations: a study of the effect of stage geometry variations, in: Proceedings of 1980 Waste Processing Conference, Washington, DC, 1980, pp. 351–359.

[2] H. Mann, Experimentelle Untersuchung, Modellierung und dynamische Simulation der mehrstufigen Partikel-Querstromklassierung, Ph.D. thesis, Otto-von-Guericke-Universität Magdeburg (2015).

[3] H. Mann, C. Roloff, T. Hagemeier, D. Thévenin, J. Tomas, Model-based experimental data evaluation of separation efficiency of multistage coarse particle classification in a zigzag apparatus, Powder technology 313 (2017) 145–160.

[4] J. Tomas, T. Gröger, C. Küchler, J. Friedrichs, Abtrennen von Wertstoffen aus Bauschutt, Chemie Ingenieur Technik 71 (6) (1999) 637–642.

[5] J. Palmer, O. R. Ghita, L. Savage, K. E. Evans, Successful closed-loop recycling of thermoset composites, Composites Part A: Applied Science and Manufacturing 40 (4) (2009) 490–498.

[6] M. Senden, Stochastic models for individual particle behavior in straight and zig zag classifiers, Ph.D. thesis, Technische Hogeschool Eindhoven (1979).

[7] T. Georgi-Maschler, B. Friedrich, R. Weyhe, H. Heegn, M. Rutz, Development of a recycling process for li-ion batteries, Journal of Power Sources 207 (2012) 173–182.

[8] F. Kaiser, Der Zickzack-Sichter - ein Windsichter nach neuem Prinzip, Chemie Ingenieur Technik 35 (4) (1963) 273–282.

[9] G. G. Rosenbrand, The separation performance and capacity of zigzag air classifiers at high particle feed rates, Ph.D. thesis, Technische Hogeschool Eindhoven (1986).

[10] J. Tomas, T. Gröger, Mehrstufige turbulente Aerosortierung von Bauschutt, Aufbereitungs-Technik 40 (8) (1999) 379–386.

[11] J. Tomas, T. Gröger, Assessment of multistage turbulent cross-flow aeroseparation of building rubble, Developments in Mineral Processing 13 (C7) (2000) 34–43.

[12] P. A. Vesilind, R. A. Henrikson, Effect of feed rate on air classifier performance, Resources and Conservation 6 (3-4) (1981) 211–221.

[13] H. Schubert, S. Böhme, T. Neeße, D. Espig, Classification in turbulent two-phase flows, in: Preprints 1st World Congress on Particle Technology, Nuremberg, Part IV, 1986, pp. 419–442.

[14] W. A. Worrell, P. A. Vesilind, Testing and evaluation of air classifier performance, Resource Recovery and Conservation 4 (3) (1979) 247 – 259.

[15] M. W. Biddulph, M. A. Connor, A method of comparing the performance of air classifiers, Resources, Conservation and Recycling 2 (4) (1989) 275–286.

[16] O. Otto, K. Hartmann, Hybrides Modell eines Sichters auf der Basis künstlicher neuronaler Netze, Chemie Ingenieur Technik 68 (12) (1996) 1578–1581.

[17] I. Gillandt, U. Fritsching, C. Riehle, Zur mehrphasigen Strömung in einem Zick-Zack-Sichter, Forschung im Ingenieurwesen 62 (11-12) (1996) 315–321.

[18] H. Glöckner, T. Hagemeier, C. Roloff, D. Thévenin, J. Tomas, Experimental investigation on the multistage particle classification in a zigzag air classifier, in: Proceedings of the World Congress on Engineering, London, Vol. II, 2014.

[19] J. Friedrich, T. Winkler, H. Lieberwirth, Numerische und experimentelle Untersuchung eines Zickzack-Sichters, Chemie Ingenieur Technik 86 (6) (2014) 906–909.

[20] C. Roloff, E. Lukas, B. van Wachem, D. Thévenin, Particle dynamics investigation by means of shadow imaging inside an air separator, Chemical Engineering Science 195 (2019) 312–324.

[21] O. Molerus, H. Hoffmann, Darstellung von Windsichtertrennkurven durch ein stochastisches Modell, Chemie Ingenieur Technik 41 (5-6) (1969) 340–344.

[22] L. Svarovsky, Solid-Liquid Separation (Third Edition), Butterworth-Heinemann, 1990.

[23] C. Roloff, H. Mann, J. Tomas, D. Thévenin, Flow investigation of a zigzag air classifier, in: the 16th International Conference on Fluid Flow Technologies, Budapest, Hungary, Vad, J., Ed., 2015, pp. 91/1–8.

[24] N. A. Zarin, Measurement of non-continuum and turbulence effects on subsonic sphere drag, Technical Report NASA-CR-1585, University of Michigan (1970).

[25] J. Kussin, M. Sommerfeld, Experimental studies on particle behaviour and turbulence modification in horizontal channel flow with different wall roughness, Experiments in Fluids 33 (1) (2002) 143–159.

List of Figures

1 Experimental test rig. 38
2 Separator modules. 39
3 Drawing of the eight-, six- and four-segment zigzag channel configurations. 40
4 Glass bead PSD. 41
5 Fluid and particle movement patterns in the ZZS. 42
6 Results of an eight-segment separation, with the parameters given in Table 5. 43
7 Direct effects of the controlled parameters. 44
8 Particle residence time and loading. 45
9 Relative cut-point settling velocity. 46
10 Separation sharpness and diffusion coefficient for the six- (▲) and eight-segment separator (♦). 47
11 Relative rise velocity against the particle loading. 48

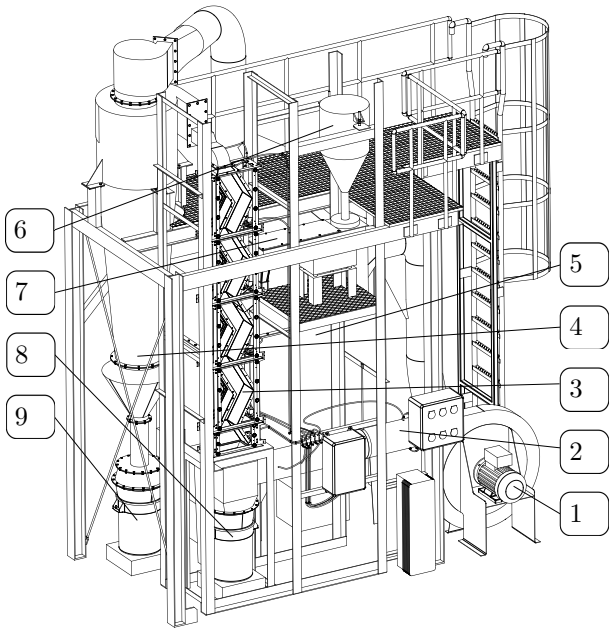
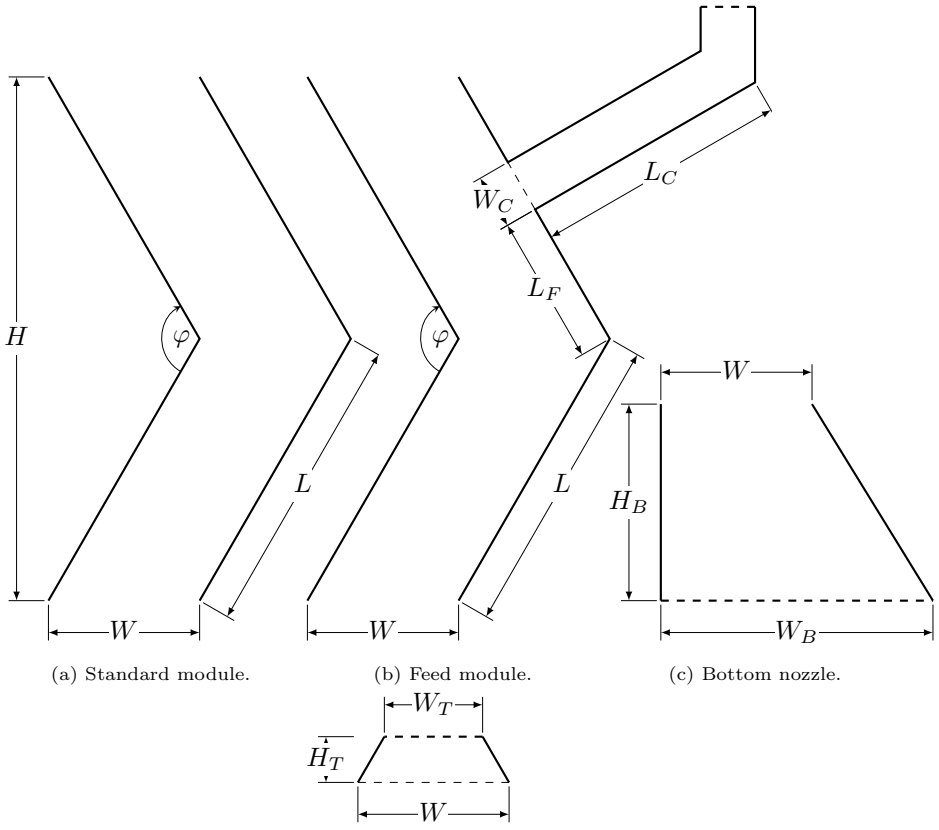


Figure 1: CAD sketch of the pilot-scale test rig with an eight-segment ZZS.



(a) Standard module. (b) Feed module. (c) Bottom nozzle.

(d) Top nozzle.

Figure 2: Contours of the pilot-scale ZZS modules, with the heights of a standard module, H, the bottom nozzle, H_B, the top nozzle, H_T; the widths of the main channel, W, the bottom nozzle, W_B, the top nozzle, W_T, the feed chute, W_C; lengths of a channel segment, L, the feed chute, L_C, the feed channel segment to the feed chute, L_F; and the bend angle, φ. The dimensions are specified in Table 2.

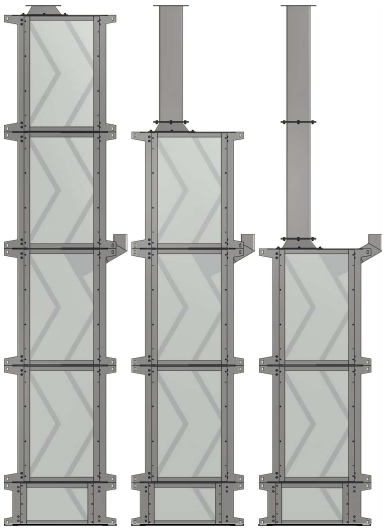


Figure 3: Drawing of the eight-, six- and four-segment zigzag channel configurations.

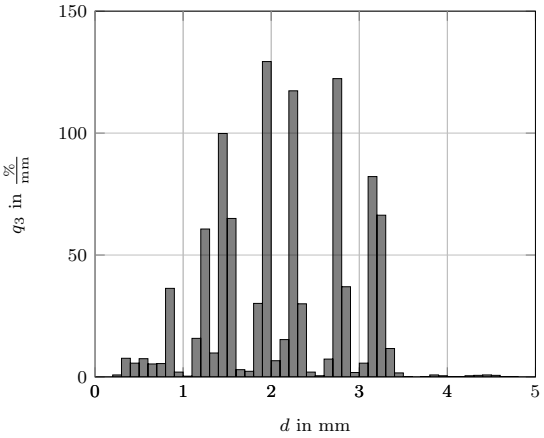
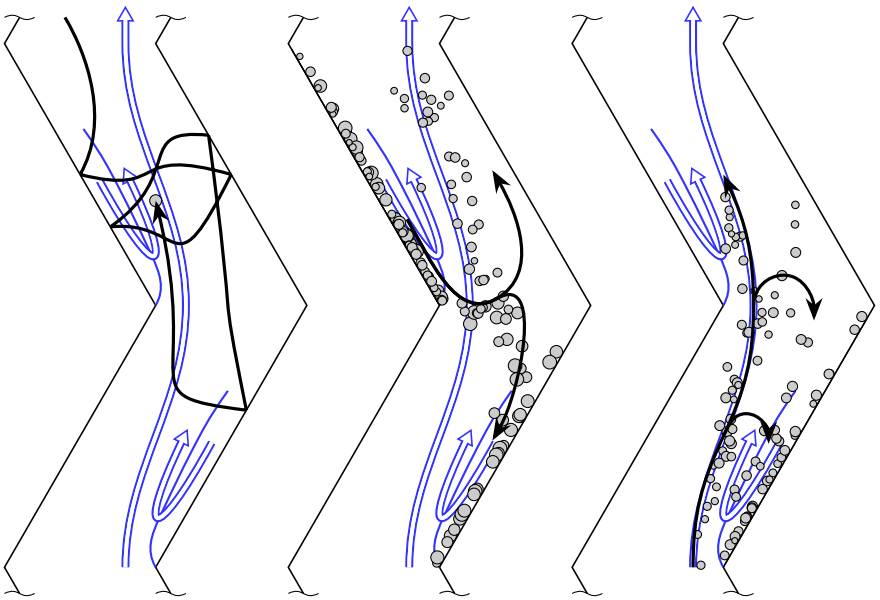


Figure 4: Initial volume-based particle size distribution (PSD) of glass beads used for experiments.

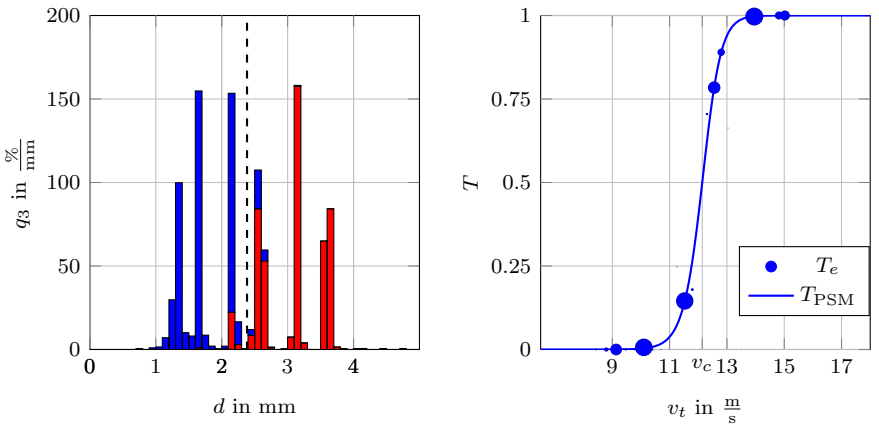


(a) Single-particle trajectory for the back and forth movement as described by Gillandt et a. [17].

(b) Separation of downwards sliding particles by the main airflow, as illustrated by Senden [6].

(c) Separation of particles rising with the main airflow.

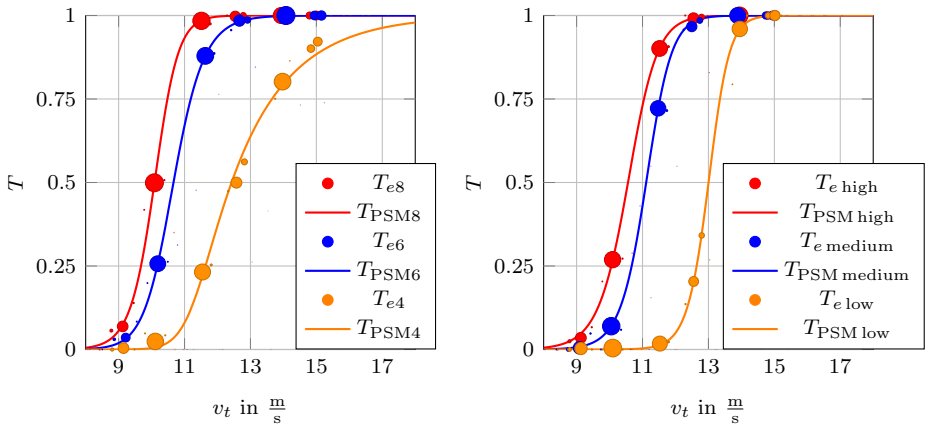
Figure 5: Observed fluid and particle movement patterns in the ZZS with the particle transport, (⟶), fluid streamlines, (⟹), backflow regions, (——), and particles, (◎). The position of the back-flow regions is according to the fluid flow measurements provided by Roloff et al. [23] for the ZZS.



(a) The stacked normalised PSDs of overflow and underflow products, $q_{3\,O}\,R_O$ (■) and $q_{3\,U}\,R_U$ (■), with the cut-point diameter, d_c (- - -).

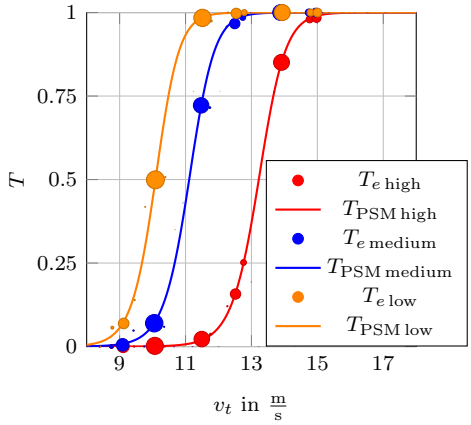
(b) Experimental grade efficiency, T_e, with marker area proportional to the weighting coefficients, w, and the fitted model, T_{PSM}.

Figure 6: Results of an eight-segment separation, with the parameters given in Table 5.



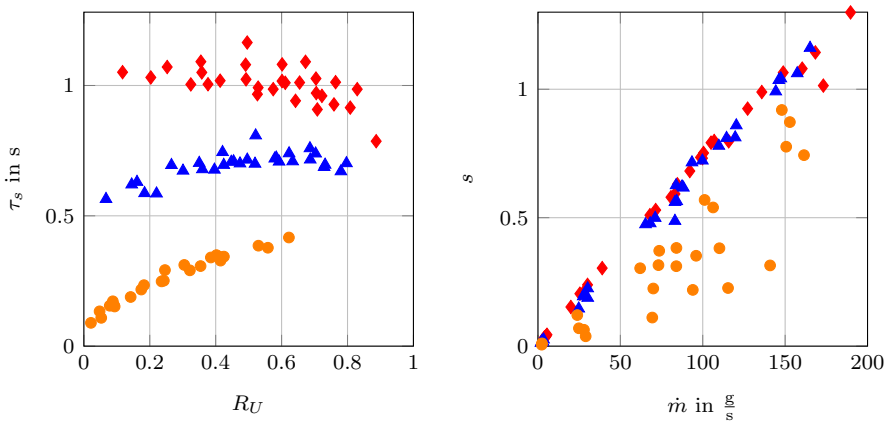
(a) Comparison of the eight-, six- and four-segment separation with constant conveyor and blower setting. Mean channel air velocity, $u = \{6.24; 6.30; 6.48\}$ m/s, feed mass stream, $\dot{m}_F = \{68; 71; 62\}$ g/s, cut-point settling velocity, $v_c = \{10.1; 10.7; 12.4\}$ m/s, and separation sharpness, $\kappa_{25\,75} = \{0.92; 0.91; 0.85\}$.

(b) Comparison of three different conveyor settings for the eight-segment separator with constant blower setting. Mean channel air velocity, $u = \{7.02; 7.06; 7.15\}$ m/s, feed mass stream, $\dot{m}_F = \{160; 100; 3.5\}$ g/s, cut-point settling velocity, $v_c = \{10.6; 11.1; 13.0\}$ m/s, and separation sharpness, $\kappa_{25\,75} = \{0.91; 0.93; 0.95\}$.



(c) Comparison of three different blower settings for the eight-segment separator with constant conveyor setting. Mean channel air velocity, $u = \{8.08; 7.06; 6.24\}$ m/s, feed mass stream, $\dot{m}_F = \{71; 100; 68\}$ g/s, cut-point settling velocity, $v_c = \{13.2; 11.1; 10.1\}$ m/s, and separation sharpness, $\kappa_{25\,75} = \{0.93; 0.93; 0.92\}$.

Figure 7: Effect of the controlled parameters (Number of channel segments, blower setting and vibration conveyor setting) onto the process parameters and the grade efficiency.



(a) Estimated mean particle residence time against the recovery of underflow product.

(b) Particle loading as a function of feed mass stream.

Figure 8: Particle residence time and loading illustrated for the separation experiments with the four- (●), six- (▲), and eight-segment separator (♦).

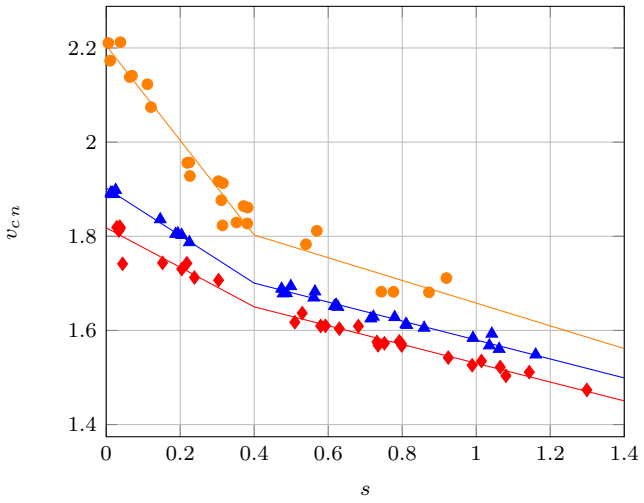
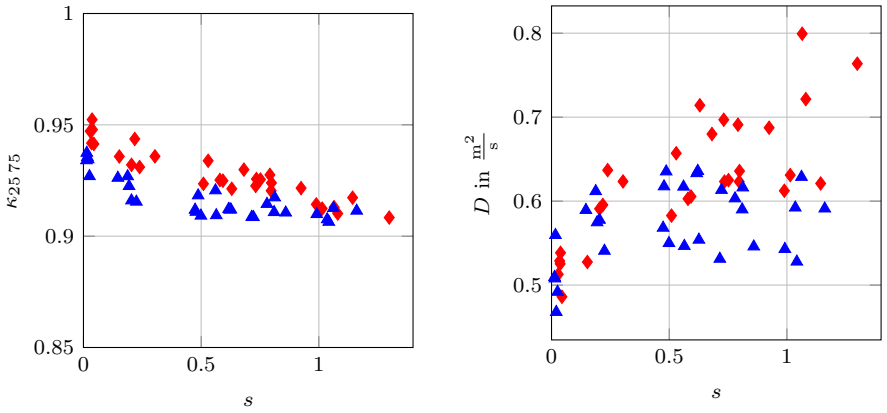


Figure 9: The relative cut-point settling velocity against the particle loading for the four- (●), six- (▲), and eight-segment separator (♦). Fits according to equation (29). Coefficients presented in Table 6.



(a) Velocity based separation sharpness as a function of particle loading.

(b) Diffusion coefficient as a function particle loading.

Figure 10: Separation sharpness and diffusion coefficient for the six- (▲) and eight-segment separator (♦).

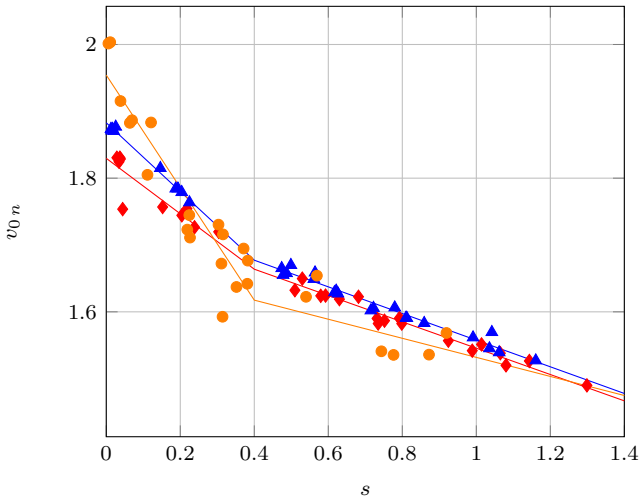


Figure 11: The relative rise velocity against the particle loading for 83 separation experiments with the four- (●), six- (▲), and eight-segment separator (♦). Fits according to equation (29). Coefficients presented in Table 7.

List of Tables

2 Dimensions of the zigzag air separator (ZZS). 50
3 Fluid and particle flow parameters for all experiments conducted in this work. 51
4 Separation result ranges. 52
5 Parameters and results for an eight-segment separation. 53
6 Relative cut-point settling velocity as function of particle loading. 54
7 Relative rise settling velocity as function of particle loading. . . . 55

Table 2: Dimensions of the zigzag air separator (ZZS).

$\varphi = 120^\circ$	$H = 700\,\mathrm{mm}$	$H_B = 260\,\mathrm{mm}$	$H_T = 60\,\mathrm{mm}$
$W = 200\,\mathrm{mm}$	$W_B = 360\,\mathrm{mm}$	$W_C = 72\,\mathrm{mm}$	$W_T = 130\,\mathrm{mm}$
$L = 404\,\mathrm{mm}$	$L_F = 198\,\mathrm{mm}$	$L_C = 336\,\mathrm{mm}$	$A = 0.0346\,\mathrm{m}^2$
$L_U = 1410\,\mathrm{mm}$	$L_{O8} = 1822\,\mathrm{mm}$	$L_{O6} = 1014\,\mathrm{mm}$	$L_{O4} = 206\,\mathrm{mm}$

Table 3: Fluid and particle flow parameters for all experiments conducted in this work.

Fluid Flow		
$1.18\,\mathrm{kg/m^3} \leq \rho_f \leq 1.23\,\mathrm{kg/m^3}$	$6.13\,\mathrm{m/s} \leq u \leq 8.46\,\mathrm{m/s}$	
Particle Flow		
$1.82\,\mathrm{g/s} \leq \dot{m}_F \leq 189.7\,\mathrm{g/s}$	$898\,\mathrm{g} \leq m_F \leq 37940\,\mathrm{g}$	$0.02 \leq R_U \leq 0.89$

Table 4: Separation result ranges: the rise velocity, v_0, the diffusion coefficient, D, the particle loading, s, the cut-point settling velocity, v_c, the settling velocity based separation sharpness, $\kappa_{25\,75}$, the diameter based separation sharpness, $\kappa_{d\,25\,75}$, the relative rise velocity, $v_{0\,n}$, the cut-point diameter, d_c, the weighted RMSE, F, the relative cut-point settling velocity, $v_{c\,n}$, and the mean particle residence time, τ_s.

$9.51\,\mathrm{m/s} \leq v_0 \leq 15.35\,\mathrm{m/s}$	$0.27\,\mathrm{m^2/s} \leq D \leq 0.80\,\mathrm{m^2/s}$	$0.0058 \leq s \leq 1.299$
$9.41\,\mathrm{m/s} \leq v_c \leq 17.51\,\mathrm{m/s}$	$0.78 \leq \kappa_{25\,75} \leq 0.95$	$0.61 \leq \kappa_{d\,25\,75} \leq 0.91$
$1.49 \leq v_{0\,n} \leq 2.00$	$1.44\,\mathrm{mm} \leq d_c \leq 4.96\,\mathrm{mm}$	$0.0036 \leq F \leq 0.044$
$1.47 \leq v_{c\,n} \leq 2.21$	$0.09\,\mathrm{s} \leq \tau_s \leq 1.16\,\mathrm{s}$	

Table 5: Parameters and results for an eight-segment separation.

Fluid Flow	$\rho_f = 1.202\,\mathrm{kg/m^3}$	$u = 6.70\,\mathrm{m/s}$	
Particle Flow	$\dot{m}_F = 3.98\,\mathrm{g/s}$	$m_F = 2387\,\mathrm{g}$	$R_U = 0.496$
Separation Evaluation	$v_0 = 12.22\,\mathrm{m/s}$	$D = 0.53\,\mathrm{m^2/s}$	$s = 0.034$
	$v_c = 12.14\,\mathrm{m/s}$	$\kappa_{25\,75} = 0.94$	$\kappa_{d\,25\,75} = 0.88$
	$v_{0\,n} = 1.82$	$d_c = 2.38\,\mathrm{mm}$	$F = 0.0058$
	$v_{c\,n} = 1.81$	$\tau_s = 1.16\,\mathrm{s}$	

Table 6: Coefficients and RMSE, F, of the relative cut-point settling velocity functions given by equation (29), which are illustrated in Figure 9.

	a	b	c	F
Four-segment	-1.005	2.2049	-0.2413	0.03054
Six-segment	-0.5046	1.902	-0.2014	0.00717
Eight-segment	-0.4200	1.818	-0.1997	0.01447

Table 7: Coefficients and RMSE of the relative rise velocity functions given by equation (29), which are illustrated in Figure 11.

	a	b	c	F
Four-segment	-0.8418	1.954	-0.1427	0.04057
Six-segment	-0.5140	1.883	-0.1994	0.006811
Eight-segment	-0.4147	1.830	-0.1970	0.01418